[5] V. Volski, P. Delmotte, and G. A. E. Vandenbosch, "Compact low cost 4 elements microstrip antenna array for WLAN," in *Proc. 7th Eur. Conf. Wireless Technology*, Amsterdam, The Netherlands, 2004, pp. 277–280.
[6] Z. Ma and G. A. E. Vandenbosch, "Low-cost wideband microstrip arrays with high aperture efficiency," *IEEE Trans. Antennas Propag.*, vol. 60, no. 6, pp. 3028–3034, Jun. 2012.
[7] P. J. Soh, G. A. E. Vandenbosch, M. Mercuri, and D. Schreurs, "Wearable wireless health monitoring: Current developments, challenges, and future trends," *IEEE Microw. Mag.*, vol. 16, no. 4, pp. 55–70, May 2015.
[8] T. Namiki, Y. Murayama, and K. Ito, "Low-cost wideband microstrip arrays with high aperture efficiency," *IEEE Trans. Antennas Propag.*, vol. 51, no. 3, pp. 478–482, Mar. 2003.

Analysis of Slotted Sectoral Waveguide Arrays With Multilayered Radomes

Mert Kalfa and Vakur B. Ertürk

***Abstract*—A method of moments/Green's function (MoM/GF) technique in the space domain is used for the rigorous and fast analysis of cylindrically conformal slotted sectoral waveguide arrays (SSWGAs) in the presence of multilayered cylindrical dielectric radomes. Representing the slots by fictitious magnetic currents via the equivalence principle, the geometry is divided into two regions and separate GF representations for each region are developed to be used in conjunction with the MoM procedure. Particularly, in the region that constitutes the cylindrically stratified medium, the newly developed closed-form GF representations for magnetic currents are valid for all source and observation points, including the source region (where source and observation points are on the top of each other). Basic performance metrics of an SSWGA such as equivalent slot currents, S-parameters, radiation patterns in the presence of a multilayered cylindrical radome are presented to assess the accuracy and efficiency of the proposed technique.**

***Index Terms*—Closed-form Green's functions (GF), conformal antennas, method of moments (MoM), slotted sectoral waveguide arrays.**

I. Introduction

Slotted sectoral waveguide arrays [SSWGAs, cylindrical counterparts of planar slotted waveguide arrays (SWGAs)] offer great potential as conformal phased array antennas in military and commercial applications for the platforms that can be locally modeled in cylindrical shapes such as the fuselage of an airplane or a missile, where stringent aerodynamic constraints, radar cross-section (RCS), and efficient use of real estate are of utmost importance. Unfortunately, their design and analysis are challenging, reported studies for the analysis of them [1]–[5] are very few with significant limitations from a full-wave analysis point of view, and the available methods for planar SWGAs [6]–[8] become insufficient in terms of both design and analysis as the curvature affects the behavior of fields significantly. Moreover, an air platform imposes strict requirements for the radome of the installed SSWGA, and most of the time many layers of composite materials are required to be placed over the slots (e.g., sandwich radomes) resulting in further complications in the design/analysis of the overall structure, which has not been reported to the best of our knowledge. Hence, the main motivation and the contribution of this communication is to present a method of moments/Green's function (MoM/GF) technique for the rigorous and fast analysis of SSWGAs in the presence of multilayered cylindrical dielectric radomes. Briefly, by invoking Schelkunoff's surface equivalence theorem, slots are represented by fictitious tangential magnetic currents and the overall geometry is divided into two regions. Interior of the sectoral waveguide forms Region I, where the GF representation reported in [4] is used and all the integrals in the associated mutual admittance matrix entries are obtained analytically, which greatly enhances the computation efficiency. The cylindrically stratified medium that models the multilayered cylindrical dielectric radome together with free-space as the outermost layer forms Region II, for which new closed-form GF (CFGF) representations are developed for tangential magnetic currents. Note that although several studies on CFGF representations for cylindrically stratified media have already been reported to be used in conjunction with MoM for the design and analysis of microstrip and slot/aperture antennas and arrays [9]–[18], they are not valid within the source region (where two current modes can partially or fully overlap during the MoM procedure). Recently, reported CFGF representations for tangential electric current modes in [19] are valid and very accurate within the source region. However, the counterpart of [19] for magnetic current modes is not available other than some preliminary works presented in [20]–[22]. Hence, another contribution of this communication is to provide new CFGF representations for tangential magnetic current modes that are valid and accurate everywhere including the source region. Finally, it should be mentioned that because of its efficiency (in particular when compared with available commercial full wave solvers), the proposed method can be combined with available optimization algorithms for the design of SSWGAs as well.

In Section II, the geometry and the formulation of the problem are presented. Section III briefly provides the evaluation of basic antenna parameters such as the radiation pattern, S-parameters, etc. Finally, numerical results for an SSWGA with a multilayered cylindrical radome are presented in Section IV to assess the accuracy and efficiency of the proposed method. An $e^{j\omega t}$ time convention, where $\omega = 2\pi f$ and f is the operating frequency, is assumed and suppressed throughout this communication.

II. Formulation

A. Geometry

The geometry of a cylindrically conformal SSWGA in the presence of multilayered cylindrical dielectric radome is illustrated in Fig. 1 together with its cross-sectional view. The geometry is divided into two regions. Region I is formed from the sectoral waveguides (SWGs) with an inner and outer radii, a_0 and a_1, respectively, while the angular span of each SWG is Φ_0 (see the cross-sectional view of Fig. 1). Each SWG is filled with a material whose constitutive parameters are ϵ_1 and μ_1. Finally, thin longitudinal (z-directed) shunt slots are introduced on the broad wall of each SWG to constitute the SSWGA as shown in Fig. 1.

Manuscript received June 29, 2015; revised October 30, 2015; accepted December 01, 2015. Date of publication December 08, 2015; date of current version February 01, 2016. This work was supported by the Turkish Scientific and Technological Research Council (TÜBİTAK) under Grant EEEAG-113E628.

M. Kalfa is with the Department of Electrical and Electronics Engineering, Bilkent University, Ankara TR-06800, Turkey, and also with Aselsan Electronics Inc., Ankara, Turkey (e-mail: kalfa@ee.bilkent.edu.tr).

V. B. Ertürk is with the Department of Electrical and Electronics Engineering, Bilkent University, Ankara TR-06800, Turkey (e-mail: vakur@ee.bilkent.edu.tr).

Color versions of one or more of the figures in this communication are available online at http://ieeexplore.ieee.org.

Digital Object Identifier 10.1109/TAP.2015.2506719

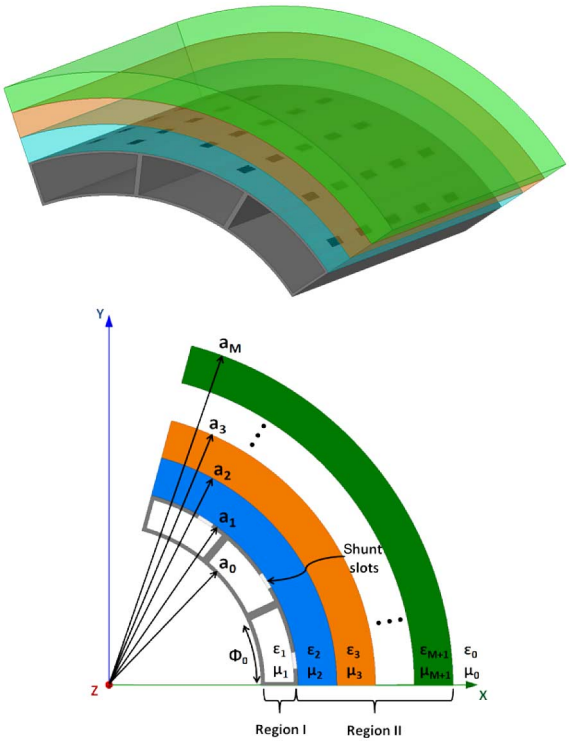

Fig. 1. Slotted sectoral waveguide array with multilayered radome.

Cylindrically stratified medium that models the multilayered cylindrical dielectric radome forms Region II as seen in Fig. 1. The innermost part of this region is assumed to be a perfect electric conductor (PEC) that forms the outer radius (a_1) of the SWG(s) with thin longitudinal shunt slots residing on it, and the outermost layer is assumed to be free-space ($\epsilon_r = 1, \mu_r = 1$). In between, an arbitrary number of material layers surrounds the PEC part coaxially. Each layer is defined by its permittivity, permeability, outer radius, and thickness denoted by ϵ_i, μ_i, a_i and $a_i - a_{i-1}$ with $i = 2, 3, 4, \ldots$, respectively. Note that the overall geometry is assumed to be infinitely long along the z-axis, and the wall thickness of waveguides is neglected.

B. Integral Equation and GFs

Replacing the thin, longitudinal slots by equivalent z-directed fictitious magnetic currents (on the inner and outer surfaces of the slots) via the surface equivalence principle and enforcing the continuity of total tangential fields over the slots, the magnetic field integral equation (MFIE) is constructed as

$$\sum_{n=1}^{N_m} \iint_{S_n} G_{zz}^{HM(I)} M_n^{(I)} \, \mathrm{d}s' - \sum_{n=1}^{\sum_m N_m} \iint_{S_n} G_{zz}^{HM(II)} M_n^{(II)} \, \mathrm{d}s' = -H_{z_{inc,n}}^{(I)} \tag{1}$$

where $\vec{M}_n^{(I)}$ and $\vec{M}_n^{(II)}$ represent the unknown currents for the nth slot in Regions I and II, respectively (with $\vec{M}_n^{(II)} = -\vec{M}_n^{(I)}$), and $G_{zz}^{HM(.)}$ is the kernel of the MFIE which relates z-directed magnetic currents to z-directed magnetic fields in Regions I and II, depending on its superscript index. For both regions, two very accurate GF representations are used that are valid for arbitrary source and observation points, and their fast evaluation significantly improves the efficiency of the overall method. Finally, $H_{z_{inc,n}}^{(I)}$ in (1) is the incident tangential magnetic field on S_n due to the TE_{11} excitation of the waveguide. Note that because the slots are electrically very narrow in the transverse direction of SWGs, equivalent magnetic currents on them are assumed to have a variation only along the z-direction and have only z components. Thus, the vector notation is omitted for simplicity purposes. Also note that since all slots are replaced with PEC surfaces (due to surface equivalence), the tangential magnetic field in Region I is found from the superposition of magnetic fields due all slot currents in the same SWG. Thus, the first summation in (1) is performed only over the slots on the same SWG, with N_m being the total number of slots in the mth SWG. However, regarding Region II, the second summation in (1) is performed over all the slot currents on all SWGs, as the tangential magnetic field in Region II (on the outer surface of a slot on an SWG) is found from the superposition of magnetic fields due to all slot currents in all SWGs.

Following a similar derivation to that of [4], $G_{zz}^{HM(I)}$ is derived and simplified for the case where both ends of the sectoral waveguide are perfectly matched (i.e., traveling wave configuration), and the final expression is given by

$$G_{zz}^{HM(I)} = j\omega\epsilon \sum_{p=0}^{\infty} \sum_{q=1}^{\infty} B_{pq} \cos(\upsilon_p \, \phi) \cos(\upsilon_p \, \phi') \times \left[\delta(z - z') - \frac{k_{c_{pq}}^2}{2jk_{z_{pq}}} e^{-jk_{z_{pq}}|z-z'|} \right] \tag{2}$$

where $\upsilon_p = p\pi/\Phi_0, \quad p = 0, 1, \ldots$ with Φ_0 being the total angular span of each sectoral waveguide in the ϕ-direction as shown in Fig. 1, and $k_{z_{pq}}^2 = k^2 - k_{c_{pq}}^2$ with $k_{c_{pq}}$ representing the cutoff wavenumbers of the SWG. They are found by solving for the qth root of the following equation for each cylindrical eigenmode index, p:

$$Y'_{\upsilon_p}(k_{c_{pq}} \, a_1) \, J'_{\upsilon_p}(k_{c_{pq}} \, a_0) - Y'_{\upsilon_p}(k_{c_{pq}} \, a_0) \, J'_{\upsilon_p}(k_{c_{pq}} \, a_1) = 0 \qquad q = 1, 2, \ldots \tag{3}$$

where $J_\upsilon(\cdot)$ and $Y_\upsilon(\cdot)$ are the first and second kind of Bessel functions, respectively, with $'$ denoting the derivative with respect to the argument. The other expressions in (2) are defined as follows:

$$B_{pq} = \frac{2}{1 + \delta_{0,p}} \frac{B_{\upsilon_p}(k_{c_{pq}} \, \rho) B_{\upsilon_p}(k_{c_{pq}} \, \rho')}{k^2 N_{pq} \Phi_0} \tag{4}$$

with $\delta_{0,p}$ being the Kronecker delta function

$$B_{\upsilon_p}(k_{c_{pq}} \, \rho) = J'_{\upsilon_p}(k_{c_{pq}} \, a_0) Y_{\upsilon_p}(k_{c_{pq}} \, \rho) - Y'_{\upsilon_p}(k_{c_{pq}} \, a_0) \, J_{\upsilon_p}(k_{c_{pq}} \, \rho) \tag{5}$$

and

$$N_{pq} = \left\{ \frac{1}{2} \rho^2 \left[\left(1 - \frac{\upsilon_p^2}{k_{c_{pq}}^2 \rho^2} \right) B_{\upsilon_p}^2(k_{c_{pq}} \, \rho) \right] \right\} \Bigg|_{a_0}^{a_1}. \tag{6}$$

Regarding the cylindrically stratified medium, $G_{zz}^{HM(II)}$ is the required component of the newly developed CFGF representations for tangential magnetic current modes that are valid and accurate everywhere including the source region. Following a similar procedure given in [19], $G_{uv}^{HM(II)}$ in space domain is expressed as

$$G_{uv}^{HM(II)} = \left(k_j^2 - \frac{\partial^2}{\partial z \partial z'} \right)^q \left(j \frac{\partial}{\partial z} \right)^m \times \left(-j \frac{\partial}{\partial \phi} \right)^{t_1} \left(j \frac{\partial}{\partial \phi'} \right)^{t_2} G_{uv2}^{HM(II)} \tag{7}$$

where the final form of $G_{uv2}^{HM(II)}$ is given by

$$\begin{aligned} G_{uv2}^{HM(II)} &= \mathcal{F}^{-1}\left\{-\frac{1}{4\omega}\sum_{n=-\infty}^{\infty} H_n^{(2)}(k_{\rho_j}\rho)J_n(k_{\rho_j}\rho')\right. \\ &\quad \left.\times\left[f_{uv}^M(n,k_z)-C_{uv}^M(k_z)\right]e^{jn(\phi-\phi')}\right\} \\ &\quad + \mathcal{F}^{-1}\left\{-\frac{1}{4\omega}\left[C_{uv}^M(k_z)-C_{uv}^M(k_{z\infty})\right]\right. \\ &\quad \left.\times\left(S_1-\left[-j\frac{2}{\pi}\log\left(\left|\beta-\beta'\right|\right)\right]\right)\right\} \\ &\quad - j\frac{2}{\pi}\log\left(\left|\beta-\beta'\right|\right) \\ &\quad \times\mathcal{F}^{-1}\left\{-\frac{1}{4\omega}\left[C_{uv}^M(k_z)-C_{uv}^M(k_{z\infty})\right]\right\} \\ &\quad - \frac{j}{4\pi\omega}C_{uv}^M(k_{z\infty})\left(I_{sing}-I'_{sing}\right) \\ &\quad - \frac{j}{4\pi\omega}C_{uv}^M(k_{z\infty})I'_{sing}. \end{aligned} \tag{8}$$

In (7), $t_1=t_2=0$ for the $uv=zz$, $t_1=0,t_2=1$ for the $uv=z\phi$ ($=\phi z$ due to reciprocity), $t_1=t_2=1$ for $uv=\phi\phi$ cases, whereas in (8), $\mathcal{F}^{-1}\{\cdot\}$ denotes the inverse Fourier transform (IFT), n is the cylindrical eigenmode, $\beta=\rho\phi$ and $\beta'=\rho'\phi'$, $k_{\rho_j}^2=k_j^2-k_z^2$ with k_j being the wavenumber of the jth medium, $S_1=H_0^2(k_{\rho_j}\left|\bar{\rho}-\bar{\rho}'\right|)$, $I_{sing}=e^{-jk_i\left|\bar{r}-\bar{r}'\right|}/\left|\bar{r}-\bar{r}'\right|$ is the same function denoted as I_1 in [19], and I'_{sing} is its problematic part (I'_1 in [19]). Finally, $C_{uv}^M(k_z)$ is the limiting value of $f_{uv}^M(n,k_z)$ (its explicit form is provided in [14]), when $n\to\infty$, and $C_{uv}^M(k_{z\infty})$ in the same equation is the value of $C_{uv}^M(k_z)$ when $k_z\to\infty$. In the final expression of the $G_{uv2}^{HM(II)}$ the first, second, and the fourth terms are calculated in closed-form via generalized pencil of function (GPOF) method [23] on a deformed path (as done in [14]) since they do not have any singularity, whereas the third (axial line singularity related term) and the fifth (space domain singularity related term) terms are calculated analytically during the mutual admittance calculations. Although, (8) is obtained for every u and v, in this work we only use $uv=zz$ case.

C. MoM Formulation and Efficient Calculation of Mutual Admittance Matrix Entries

In (1), expanding $M_n^{(\cdot)}$ on each slot at $\rho'=a_1$ with a finite set of $2z_a\times 2\beta_a$ sized z-directed piecewise sinusoidal (PWS) basis functions and using a Galerkin MoM solution, the following matrix equation is obtained:

$$\left[\overline{\overline{Y_{ij}^{(I)}}}+\overline{\overline{Y_{ij}^{(II)}}}\right]\begin{bmatrix}\alpha_1\\ \vdots\\ \alpha_N\end{bmatrix}=\begin{bmatrix}I_1\\ \vdots\\ I_N\end{bmatrix} \tag{9}$$

where α_j is the unknown amplitude of the PWS current mode K_j; $Y_{ij}^{(I)}$ and $Y_{ij}^{(II)}$ denote the mutual admittance matrix entries for Regions I and II, respectively, and are given by

$$Y_{ij}^{(I)}=\begin{cases}\iint\limits_{S_i}\iint\limits_{S_j} G_{zz}^{HM(I)}K_iK_j\mathrm{d}s\mathrm{d}s', & K_i,K_j\in\text{same WG}\\ 0, & \text{otherwise}\end{cases} \tag{10}$$

$$Y_{ij}^{(II)}=\iint\limits_{S_i}\iint\limits_{S_j} G_{zz}^{HM(II)}K_iK_j\,\mathrm{d}s\mathrm{d}s' \tag{11}$$

and finally, $I_i^{(I)}$ represents the entries of the excitation vector given by

$$I_i^{(I)}=-\iint\limits_{S_i} H_{z_{inc,i}}^{(I)}K_i\,\mathrm{d}s. \tag{12}$$

In addition to the efficient calculation of the GF representations for both regions, the efficiency of the proposed method is further improved by evaluating all integration parts of the mutual admittance entries for Region I, given by (10), as well as the excitation vector entries, given by (12), analytically. Briefly, because $G_{zz}^{HM(I)}$ given in (2) is formed from two terms, $Y_{ij}^{(I)}$ in (10) is rewritten as

$$Y_{ij}^{(I)}=\begin{cases}Y_{ij,A}^{(I)}+Y_{ij,B}^{(I)}, & K_i,K_j\in\text{same WG}\\ 0, & \text{otherwise}\end{cases} \tag{13}$$

where the final form of each term in (13) is given by

$$Y_{ij,A}^{(I)}=-\sum_{p=0}^{\infty}\sum_{q=1}^{\infty}j\omega\epsilon B_{pq}\frac{k_{c_{pq}}^2}{2jk_{z_{pq}}}I_\beta I_{z,A} \tag{14}$$

$$Y_{ij,B}^{(I)}=\sum_{p=0}^{\infty}\sum_{q=1}^{\infty}j\omega\epsilon B_{pq}I_\beta I_{z,B} \tag{15}$$

with

$$I_\beta=\frac{4a_1^2}{\upsilon_p^2}\cos\left(\frac{\upsilon_p}{a_1}\beta_i\right)\cos\left(\frac{\upsilon_p}{a_1}\beta_j\right)\sin^2\left(\frac{\upsilon_p}{a_1}\beta_a\right). \tag{16}$$

Regarding the evaluation of $I_{z,A}$ and $I_{z,B}$, the following three different cases are considered based on the relative positions of z_i and z_j (center coordinates of the ith and jth current modes along the z-direction, respectively).

1) $z_i\le z_j-2z_a$ case: $I_{z,B}=0$ leading to $Y_{ij,B}^{(I)}=0$ and $Y_{ij}^{(I)}=Y_{ij,A}^{(I)}$. Thus, calculating $I_{z,A}$ in closed-form, the final expression for $Y_{ij}^{(I)}$ becomes

$$\begin{aligned} Y_{ij}^{(I)} &= -\sum_{p=0}^{\infty}\sum_{q=1}^{\infty}\omega\epsilon B_{pq}\frac{k_{c_{pq}}^2}{k_{z_{pq}}}\frac{e^{\,jk_{z_{pq}}(z_i-z_j)}}{\beta_a^2\sin^2\left(k_a\,z_a\right)}\frac{I_\beta}{2} \\ &\quad\times\left[\frac{k_a}{k_{z_{pq}}^2-k_a^2}\left(\cos(k_a\,z_a)-\cos(k_{z_{pq}}\,z_a)\right)\right]^2. \end{aligned} \tag{17}$$

2) $z_i=z_j$ case: This is the case where two current modes are fully overlapped, and the final forms of $I_{z,A}$ and $I_{z,B}$ are obtained in closed form as

$$\begin{aligned} I_{z,A} &= \frac{1}{2\beta_a^2\sin^2(k_az_a)}\left\{I_-^2+\frac{2}{k_{z_{pq}}^2-k_a^2}\right. \\ &\quad\times\left[-k_ae^{-jk_{z_{pq}}z_a}I_+ +\frac{1}{4}\left(1-\cos(2k_az_a)\right)\right. \\ &\quad\left.\left.+\frac{jk_{z_{pq}}}{4}\left(\frac{\sin(2k_az_a)}{k_a}-2z_a\right)\right]\right\} \end{aligned} \tag{18}$$

$$I_{z,B}=\frac{1}{4\beta_a^2\sin^2\left(k_a\,z_a\right)}\left[z_a-\frac{\sin(2k_az_a)}{2k_a}\right]. \tag{19}$$

3) $z_i=z_j-z_a$ case: This is the case where two current modes are partially overlapped along the z-axis, and the final forms of $I_{z,A}$ and $I_{z,B}$ are obtained in closed form as

$$I_{z,A} = \frac{1}{4\beta_a^2 \sin^2(k_a\ z_a)} \Big\{ e^{-jk_{z_{pq}} z_a} \left(I_-^2 + 2I_- I_+\right) + \frac{1}{k_{z_{pq}}^2 - k_a^2} \Big[-k_a I_- + e^{-jk_{z_{pq}} z_a} I_+ \left(k_a \cos(k_a\ z_a) + jk_{z_{pq}} \sin(k_a\ z_a)\right) + jk_{z_{pq}} z_a \cos(k_a\ z_a) - \frac{jk_{z_{pq}}}{k_a} \sin(k_a\ z_a) \Big] \Big\} \quad (20)$$

$$I_{z,B} = \frac{1}{8\beta_a^2 \sin^2(k_a\ z_a)} \left(\frac{\sin(k_a z_a)}{k_a} - z_a \cos(k_a z_a) \right) \quad (21)$$

where

$$I_\pm = \frac{k_a \cos(k_a\ z_a) \pm jk_{z_{pq}} \sin(k_a\ z_a) - k_a e^{-jk_{z_{pq}} z_a}}{k_{z_{pq}}^2 - k_a^2}. \quad (22)$$

Regarding the evaluation of (11) for $uv = zz$, the procedure outlined in [19] is used.

D. Excitation Vector Entries

Only the fundamental TE_{11} mode is assumed to be excited inside the SWG (although an arbitrary number of modes could be incorporated in the analysis). Hence, using the z-component of the magnetic field, H_z, due to the TE_{11} excitation given in [3], the final closed-from expression of $I_i^{(I)}$ is obtained for $p = q = 1$ as

$$I_i^{(I)} = -\frac{a_1 k_{c11}^2 B_{\upsilon_1}(k_{c_{11}}\rho) e^{-jk_{z_{11}} z_i}}{j\omega\mu\upsilon_1 \beta_a J'_{\upsilon_1}(k_{c_{11}}\ a_0) \sin(k_a\ z_a)} \times \cos\left(\frac{\upsilon_1}{a_1}\ \beta_i\right) \sin\left(\frac{\upsilon_1}{a_1}\ \beta_a\right) (I_- + I_+) \quad (23)$$

where $I_\pm$ is defined in (22).

III. Evaluation of Basic Antenna Parameters

The equivalent currents obtained from the solution of (9) are used to evaluate basic antenna parameters such as far-zone copolarized radiation patterns, realized gain, and S-parameters in the presence of multilayered cylindrical dielectric radomes.

The far-zone copolarized (ϕ-directed) electric fields are calculated from the z-directed equivalent magnetic currents in Region II using $G_{\phi z}^{EM(II)}$ in the cylindrically stratified medium, where the source is at $\rho' = a_1$ and the fields are calculated at the observation point (ρ) when $\rho \to \infty$. Briefly, starting with the spectral domain representation of $G_{\phi z}^{EM(II)}$ given in [9] and using the large argument approximation of the Hankel function due to $\rho \to \infty$, and then transforming it to the space domain by using the stationary phase method (for the IFT part), the final form of the GF for the far-zone copolarized electric field is obtained as

$$G_{\phi z_{FF}}^{EM(II)}(\xi, \phi) = \frac{e^{j\pi/4}}{\sqrt{2\pi}} \frac{1}{k_0 \sin\theta} \tilde{G}_0(\xi, \phi) \quad (24)$$

where

$$\tilde{G}_0(\xi, \phi) = -\frac{e^{j\frac{\pi}{4}}}{\sqrt{2\pi}} (k_2^2 - \xi^2) \frac{\mu_M}{\mu_2} \times \sum_{n=0}^{\infty} \frac{1}{1 + \delta_{0n}} \cos(n\phi)\ e^{jn\frac{\pi}{2}} \overline{\mathbf{F}}_0(2,2) \quad (25)$$

with ξ being $k_0 \cos\theta$ that corresponds to the stationary phase point along k_z, and $\overline{\mathbf{F}}_0$ is a 2×2 matrix defined as

$$\overline{\mathbf{F}}_0 = \tilde{\overline{\mathbf{T}}}_{2,M} \tilde{\overline{\mathbf{M}}}_{2+} \left[J_n(k_{\rho_2}\rho') \overline{\mathbf{I}} + H_n^{(2)}(k_{\rho_2}\rho') \tilde{\overline{\mathbf{R}}}_{2,1} \right]. \quad (26)$$

All terms in (26) are explicitly defined in [9]. Note that in (24)–(26), the subscript M indicates the outermost air layer index (i.e., $\epsilon_M = \epsilon_0$, $\mu_M = \mu_0$), and the subscript 2 denotes the source layer index, where the source is at the PEC-first dielectric interface. Also note that the e^{-jkr}/r term is neglected to normalize the distance to 1 m in SI units. Finally, the total radiation from an SSWGA is found by integrating (24) over the surface where all equivalent currents in Region II exist, and the resultant expression can be used to calculate the realized gain. A similar approach can be followed to obtain cross-polarized far-zone electric fields, which would provide further information on the antenna performance.

S-parameters are calculated by decomposing the magnetic field, H_z, due to the equivalent magnetic currents in Region I of an SSWGA into forward and backward scattered waves, which contribute to the reflection and transmission coefficients in their respective waveguides. Assuming the fundamental TE_{11} mode is the only propagating mode in the waveguide and making use of (2), H_z is calculated at the predefined reference planes (such as excitation ports or loads), which are located sufficiently far enough from the slots to ensure that only the TE_{11} mode waves exist on the reference planes, and all other higher order modes are highly attenuated due to being evanescent modes. As a result, a backward or forward scattered TE_{11} field coefficient is defined as the ratio of (2) evaluated at $z \neq z'$ for $(p, q) = (1, 1)$, and a unit amplitude TE_{11} excitation given in [3], and is given by

$$C_{11} = -j \frac{J'_{\upsilon_1}(k_{c11} a_0) B_{\upsilon_1}(k_{c11} a_1)}{N_{11} \Phi_0 k_{z_{11}}} \cos(\upsilon_1\ \phi'). \quad (27)$$

Finally, the total backward and/or forward scattered waves at the reference planes are found by integrating (27) over the surface where all equivalent currents in Region I exist. The whole S-matrix of the SSWGA can be calculated by repeating this process for each individual waveguide excitation.

IV. Numerical Results

An SSWGA formed from three identical air-filled ($\epsilon_1 = \epsilon_0$, $\mu_1 = \mu_0$) SWGs together with an A-type sandwich radome (skin-core-skin), which is placed 5 mm away from the SSWGA, is analyzed with the proposed MoM/GF technique and the numerical results are compared to the results obtained from HFSS™ simulations to assess the accuracy and efficiency of the method. The geometrical details of the analyzed SSWGA are as follows: $a_0 = 20$ mm, $a_1 = 30.16$ mm, $\Phi_0 = 52^\circ$, SWGs are placed 55° apart from each other, and both ends of the SWGs are perfectly matched (traveling-wave case). Also, there are 8 identical slots on each SWG (total of 24 slots in the array), each slot has a size of (14 mm, 0.5 mm) and 9 overlapping PWS current modes are used to expand the current on each slot. Besides, the slots are placed 20 mm apart along z-axis, and reference planes are located 100 mm from the nearest slot center. Finally, the radome skins are 0.83 mm thick with $\epsilon_r = 4.3$, which represent a stack of glass fiber fabrics and the core is 8 mm thick with $\epsilon_r = 1.09$, which represents a foam or honeycomb material with electrical properties close to air. The resulting geometry, together with the enumeration of the waveguide ports, is shown in Fig. 2.

100 p-modes and 100 q-modes are taken into account to calculate $G_{zz}^{HM(I)}$ in (2), whereas $N_1 = 150$, $N_2 = 150$, $N_3 = 50$ spectral domain samples on the deformed path defined by $T_1 = 0.1$, $T_2 = 20$, $T_3 = 22$ are approximated by $M_1 = 5$, $M_2 = 5$, $M_3 = 1$ complex exponentials to obtain the CFGF representations for $G_{zz2}^{HM(II)}$. Finally, only the first 200 cylindrical eigenmodes (n) are taken. It should

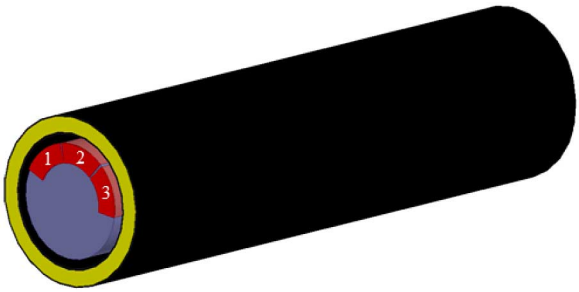

Fig. 2. HFSS model of the SSWGA with an A-sandwich radome.

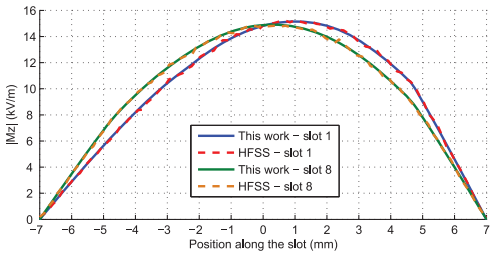

Fig. 3. Equivalent slot magnetic current magnitudes for SWG-1 under 1W excitation at 10 GHz.

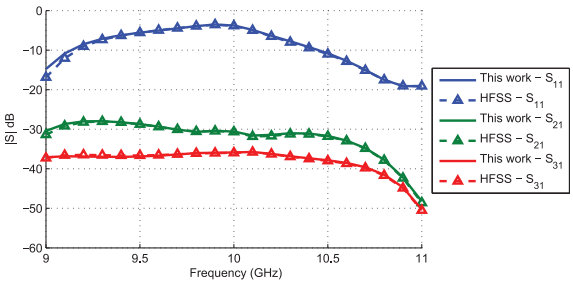

Fig. 4. S-parameters.

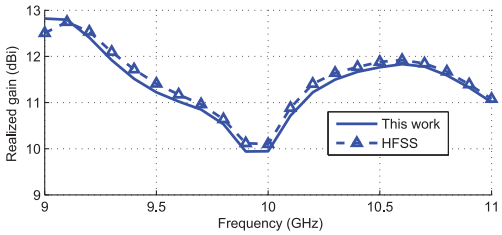

Fig. 5. Active array realized gain at boresight ($\theta = 90°, \phi = 0°$).

be noted that 200 cylindrical eigenmodes (as well as 100 p- and 100 q-modes) are actually larger than what is necessary for the convergence of the summations (including the self-terms) but chosen as are to leave a safety margin.

Numerical results in the form of equivalent magnetic current amplitudes, S-parameters, realized gain, and radiation patterns and their comparison with those obtained from HFSS^{TM} simulations are shown in Figs. 3–6. The magnetic current amplitudes given in Fig. 3 belong to the first and last slots of the first SWG, while only the first SWG is excited with a power of 1 W at 10 GHz. On the other hand, the realized gain and radiation patterns are calculated when all three SWGs are excited uniformly. The realized gain in Fig. 5 is given at the antenna boresight ($\theta = 90°, \phi = 0°$).

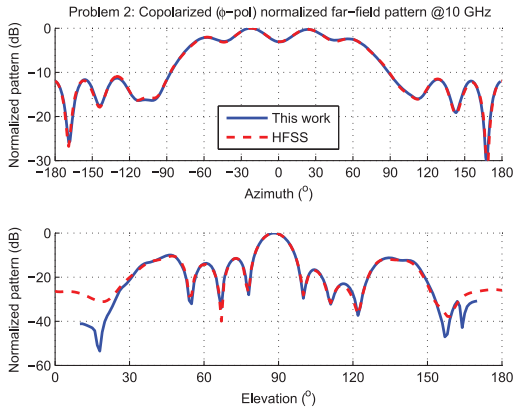

Fig. 6. Copolarized (ϕ-directed) normalized E-plane (azimuth) and H-plane (elevation) radiation patterns.

Results obtained from the proposed MoM/GF technique agree very well with that of HFSS^{TM}, which demonstrates the accuracy of the proposed method. The only discrepancy is observed in the radiation patterns when the observation angle is close to the axis of the cylinder due to the fact that the proposed method assumes the geometry is infinitely long along the axis of the cylinder (i.e., z-direction), whereas in HFSS^{TM} the geometry must be finite and is 660-mm long along the same direction. However, if the first and final slots are sufficiently far away from the ends of the cylinder along the axis of the cylinder, this discrepancy becomes less visible. Regarding the efficiency, the proposed method offers a much faster solution with significant reduction in required computer resources. HFSS^{TM} simulations are performed in a high performance computer (HPC), with 512-cores and 4 TBs of RAM.128 cores and 140 GB RAM are used and it takes 110 min/frequency when available acceleration algorithms such as domain decomposition and parallel processing are utilized to increase the efficiency of the simulations. On the other hand, using MATLAB, the proposed method is implemented in a modest desktop computer with a Core2Duo processor and 2 GBs of RAM. It uses only 0.8 GB RAM and lasts less than 3 min/frequency.

V. Conclusion

A fast and accurate MoM/GF technique in the space domain is presented for the rigorous analysis of SSWGAs with multilayered radomes (modeled as cylindrically stratified media). Numerical results due to an SSWGA with a sandwich type radome confirm both accuracy and efficiency of the technique. Thus, when compared with available commercial full wave solvers, it can be combined with available optimization algorithms for the design of SSWGAs as well.

References

[1] F. Lin and A. Omar, "Segment-sector waveguides," in *Proc. IEEE Int. Symp. Antennas Propag. (AP-S/URSI)*, San Josa, CA, USA, Jun. 1989, pp. 965–968.

[2] S.-W. Lue, S.-C. Li, and S.-M. Cao, "Slot antenna in the curved broad wall of a sectoral waveguide," in *Proc. Asia-Pacific Microwave Conf., (APMC 92)*, Adelaide, Australia, Aug. 1992, vol. 1, pp. 401–403.

[3] S.-W. Lue, Y. Zhuang, and S.-M. Cao, "The equivalent parameters for the radiating slot on a sectoral waveguide," *IEEE Trans. Antennas Propag.*, vol. 42, no. 11, pp. 1577–1581, Nov. 1994.

[4] G.-X. Fan and J.-M. Jin, "Scattering from a cylindrically conformal slotted waveguide array antenna," *IEEE Trans. Antennas Propag.*, vol. 45, no. 7, pp. 1150–1159, Jul. 1997.

[5] M.-P. Jin, M.-Q. Qi, W. Wang, and X.-L. Liang, "Design of a cylindrical conformal waveguide-fed slot array antenna," in *Proc. IEEE Int. Symp. Antennas Propag. (AP-S/URSI)*, Memphis, TN, USA, Jul. 2014, pp. 1053–1054.
[6] R. S. Elliott, "An improved design procedure for small arrays of shunt slots," *IEEE Trans. Antennas Propag.*, vol. 31, no. 1, pp. 48–53, Jan. 1983.
[7] L. G. Josefsson, "Analysis of longitudinal slots in rectangular waveguides," *IEEE Trans. Antennas Propag.*, vol. 35, no. 12, pp. 1351–1357, Dec. 1987.
[8] P. Katehi, "Dielectric-covered waveguide longitudinal slots with finite wall thickness," *IEEE Trans. Antennas Propag.*, vol. 38, no. 7, pp. 1039–1045, Jul. 1990.
[9] Ç. Tokgöz, and G. Dural, "Closed-form Green's functions for cylindrically stratified media," *IEEE Trans. Microw. Theory Tech.*, vol. 48, no. 1, pp. 40–49, Jan. 2000.
[10] J. Sun, C.-F. Wang, L.-W. Li, and M.-S. Leong, "Further improvement for fast computation of mixed potential Green's functions for cylindrically stratified media," *IEEE Trans. Antennas Propag.*, vol. 52, no. 11, pp. 3026–3036, Nov. 2004.
[11] M. He and X. Xu, "Closed-form solutions for analysis of cylindrically conformal microstrip antennas with arbitrary radii," *IEEE Trans. Antennas Propag.*, vol. 53, no. 1, pp. 518–525, Jan. 2005.
[12] Ş. Karan, V. B. Erturk, and A. Altintas, "Closed-form Green's function representations in cylindrically stratified media for method of moments applications," *IEEE Trans. Antennas Propag.*, vol. 57, no. 4, pp. 1158–1168, Apr. 2009.
[13] J. Wu, S. K. Khamas, and G. G. Cook, "An efficient asymptotic extraction approach for the Green's functions of conformal antennas in multilayered cylindrical media," *IEEE Trans. Antennas Propag.*, vol. 58, no. 11, pp. 3737–3742, Nov. 2010.
[14] M. S. Akyuz, V. B. Erturk, and M. Kalfa, "Closed-form Green's function representations for mutual coupling calculations between apertures on a perfect electric conductor circular cylinder covered with dielectric layers," *IEEE Trans. Antennas Propag.*, vol. 59, no. 8, pp. 3094–3098, Aug. 2011.
[15] L.-F. Ye, F. Zhao, K. Xiao, and S.-L. Chai, "A robust method for the computation of Green's functions in cylindrically stratified media," *IEEE Trans. Antennas Propag.*, vol. 60, no. 6, pp. 3046–3051, Jun. 2012.
[16] L.-F. Ye, S.-L. Chai, H.-S. Zhang, D. Peng, and K. Xiao, "Solving the axial line problem for fast computation of mixed potential Green's functions in cylindrically stratified media," *IEEE Trans. Antennas Propag.*, vol. 61, no. 1, pp. 23–37, Jan. 2013.
[17] J. Wu, S. K. Khamas, and G. G. Cook, "Moment method analysis of a conformal curl antenna printed within layered dielectric cylindrical media," *IEEE Trans. Antennas Propag.*, vol. 61, no. 7, pp. 3912–3917, Jul. 2013.
[18] Z. Jin, Y. Jiang, L. Ye, H. Yang, and K. Xiao, "Accurate calculation of mutual coupling between apertures on a large coated cylinder using mixed potential Green's functions," *IEEE Trans. Antennas Propag.*, vol. 62, no. 9, pp. 4841–4846, Sep. 2014.
[19] Ş. Karan and V. B. Ertürk, "Analysis of input impedance and mutual coupling of microstrip antennas on multilayered circular cylinders using closed-form Green's function representations," *IEEE Trans. Antennas Propag.*, vol. 62, no. 11, pp. 5485–5496, Nov. 2014.
[20] M. Kalfa and V. B. Ertürk, "Derivations of Green's function representations for the analysis of sectoral waveguides embedded in cylindrically stratified media," in *Proc. IEEE Int. Symp. Antennas Propag. (AP-S/URSI)*, Orlando, FL, USA, Jul. 2013 pp. 172.
[21] M. Kalfa and V. B. Ertürk, "Design and analysis of slotted sectoral waveguide array antennas embedded in cylindrically stratified media," in *Proc. IEEE Int. Symp. Antennas Propag. (AP-S/URSI)*, Memphis, TN, USA, Jul. 2014, pp. 146.
[22] M. Kalfa, S. Karan, and V. B. Ertürk, "Analysis of cylindrically conformal antennas using closed-form Green's function representations," in *9th Eur. Conf. Antennas and Propag. (EuCAP'15)*, Lisbon, Portugal, Apr. 2015, pp. 1–4.
[23] Y. Hua and T. K. Sarkar, "Generalized pencil-of-function method for extracting poles of an EM system from its transient response," *IEEE Trans. Antennas Propag.*, vol. 37, no. 2, pp. 229–234, Feb. 1989.

A Wide-Angle Scanning and Low Sidelobe Level Microstrip Phased Array Based on Genetic Algorithm Optimization

Ya-Qing Wen, Bing-Zhong Wang, and Xiao Ding

***Abstract*—In order to obtain a wide-angle scanning and low sidelobe level (SLL) microstrip phased array with a finite metal ground, a novel microstrip phased array based on microstrip magnetic dipole is presented in this communication. Microstrip magnetic dipoles are employed as the driven elements in the phased array. Meanwhile, coupling patches are embedded between the adjacent driven elements, and coupling energy is transferred between driven elements by the coupling patches. Strong coupling has been constructed between elements as the driven element spacing is only about $0.35\ \lambda$. With the influence of adjacent elements, the 3-dB beamwidth (BW) of each active element can reach over $\pm 80^\circ$ in the elevation plane. From simulation and measurement, the main lobe scanning ranges of an 8-element and a 16-element phased arrays can both extend over $\pm 80^\circ$ in the elevation plane with a gain fluctuation less than 3 dB. Furthermore, in order to keep the SLL low in the scanning, especially at the low elevation angles, genetic algorithm (GA) has been used, and the SLL has been decreased to the value of -9 dB in the full scanning range of $\pm 77^\circ$ for the eight-element array.**

***Index Terms*—Genetic algorithm (GA), low sidelobe level (SLL), microstrip magnetic dipole, phased array, wide-angle scanning.**

I. Introduction

Phased array has been widely used in military radars and civilian satellite communications, to name a few, because of its unique characteristics of scanning without inertia [1], [2]. In recent years, researchers pay more attention on the method of extending phased array's scanning range and beamforming of radiation pattern while scanning. Normally, there are two effective methods to obtain large scanning range. First, a phased array with wide 3-dB beamwidth (BW) elements can achieve a large scanning range. Wide-angle scanning phased array with pattern reconfigurable elements is one of typical examples [3]–[5]. In [5], the whole scanning area was divided into several subareas according to the reconfigurable elements' different reconfigurable modes. The results showed that the corresponding phased array with reconfigurable elements can extend the scanning range of the main lobe over $\pm 70^\circ$ with a gain fluctuation less than 3 dB. Besides, mutual coupling between elements is another important factor for scanning. With the production of coupling energy, radiation performance, such as gain, sidelobe level (SLL), and efficiency, will worsen, especially at low elevation angles. Therefore, many researchers choose the way of suppressing mutual couple effects to achieve better scanning. However, the mutual coupling energy can be utilized in the phased array to enhance the scanning performance [6]. The authors setup a three-patch subarray,

Manuscript received January 12, 2015; revised October 02, 2015; accepted December 06, 2015. Date of publication December 09, 2015; date of current version February 01, 2016. This work was supported in part by the National Natural Science Foundation of China under Grant 61331007, Grant 61361166008, and Grant 61401065, in part by the Specialized Research Fund for the Doctoral Program of Higher Education of China under Grant 20120185130001, and in part by the EHF Key Laboratory of Fundamental Science Project A03010023801171003.

The authors are with the Institute of Applied Physics, University of Electronic Science and Technology of China, Chengdu 610054, China (e-mail: yaqingwen123@gmail.com; bzwang@uestc.edu.cn; xding@uestc.edu.cn).

Color versions of one or more of the figures in this communication are available online at http://ieeexplore.ieee.org.

Digital Object Identifier 10.1109/TAP.2015.2507173